Applied Physics Letters

Reliability of cancer cell elasticity in force microscopy

Cite as: Appl. Phys. Lett. **116**, 083701 (2020); https://doi.org/10.1063/1.5143432
Submitted: 24 December 2019 . Accepted: 10 February 2020 . Published Online: 26 February 2020

Anahid Amiri, Florian D. Hastert, Lars-Oliver Heim, and Christian Dietz

Applied Physics Letters ARTICLE scitation.org/journal/apl

Reliability of cancer cell elasticity in force microscopy

Cite as: Appl. Phys. Lett. **116**, 083701 (2020); doi: 10.1063/1.5143432
Submitted: 24 December 2019 · Accepted: 10 February 2020 ·
Published Online: 26 February 2020

Anahid Amiri,[1,a)] Florian D. Hastert,[2] Lars-Oliver Heim,[1] and Christian Dietz[1,a)]

AFFILIATIONS

[1]Physics of Surfaces, Institute of Materials Science, Technische Universität Darmstadt, Alarich-Weiss-Str. 2, 64287 Darmstadt, Germany
[2]Cell Biology and Epigenetics, Department of Biology, Technische Universität Darmstadt, 64287 Darmstadt, Germany

[a)]**Electronic addresses:** anahid.amiri@stud.tu-darmstadt.de and dietz@pos.tu-darmstadt.de

ABSTRACT

Evaluating the mechanical properties of biological cells in their living state is of upmost importance for understanding cellular behavior in health or disease and in particular cancer cells. In recent years, force microscopy and spectroscopy have become inevitable tools to attain the elastic modulus of cells as a whole using colloidal probes or with high lateral precision by sharp tips. However, the obtained values have to be treated with due care to avoid data misinterpretation. Here, we present a comparison of elasticity between four metastatic cancer cell lines (lung, liver, skin, and breast epithelial-type cancer cells) taken by colloidal and sharp probes using force spectroscopy on cell monolayers and stress the impact of a stiff substrate, which cells are attached to, on the measured values especially in cancerous cells, which depict abnormalities in structure and cellular components. As a result of our analysis, we suggest to solely use sharp probes for the mechanical characterization of cancer cells when the force-distance relation is fit by a conventional contact mechanics model such as the Hertz model.

Alterations of mechanical properties of cells and biological tissues are associated with cell processes and diseases.[1–11] Evaluating stiffness values on monolayers of cells is full of ambiguity, specifically when it comes to cancerous cells, which show abnormalities in the structure and makeup of cellular components, for example, a scarce amount of cytoplasm, enlarged prominent nuclei, and a variety of shapes and cytoskeleton malformations. Many studies on elastic moduli of healthy and cancerous cells have been performed by colloidal and sharp-tip probes on multilayers of cells or cell-extracellular matrices attached to a stiff substrate using semi-infinite contact mechanics models,[2,12,13] which do not raise the concern of neglecting the substrate stress reflection using these contact mechanics models in the determination of elastic modulus.[14] Furthermore, similar experiments were performed on monolayers of cells using different algorithms to obtain mechanical properties[15,16] in particular from amplitude and phase lag by dynamic modes.[17,18] Nevertheless, there are studies on monolayers of cells using methods such as PeakForce tapping (PFT) at which the negligence of the impact of substrate reflection or the physiological condition of the compared cells leads to data misinterpretation. In this Letter, we focused on measuring the stiffness values of monolayers of four epithelial-type carcinoma-derived cell lines (BT20, HS695T, Calu_1, and PLC/PRF/5) grown on glass cover slides by using colloidal and sharp-tip probes to receive a richer picture of the stress reflection problem in AFM measurements and to suggest an accurate method and analysis for the elastic moduli measurement on monolayers of living cells using conventional mechanics models. One of the most common contact mechanics models traditionally used by scientists for elastic characterization is the Hertz/Sneddon model that provides simple access to the force-indentation relationship between the probe and the sample, e.g., for a conical intender

$$F_L = \frac{2}{\pi}\frac{E}{1-\upsilon^2}\tan(\alpha)\delta^2, \tag{1}$$

where F_L is the applied load of the indenter, E the elastic modulus of the sample, υ the sample's Poisson ratio, α the half opening angle of the cone, and δ the indentation depth. If the force-distance relationship is recorded by nanomechanical spectroscopy in high-lateral resolution as for the PeakForce tapping mode deployed in this study, then maps of the elastic modulus E can be extracted fitting equation (1) to each curve. We note that the model is based on purely elastic interactions and thus does not consider viscous effects between the indenter and the sample.

Invasive ductal carcinoma cell line BT-20, amelanotic melanoma cell line HS695T, liver hepatoma cell line PLC/PRF/5, and human

lung cancer cell line Calu_1 were used in this study and received in our laboratory from CLS Cell Lines Service GmbH (Eppelheim, Germany). For having the same culturing condition, all four cell lines were cultured at the first stage in a Petri flask in Dulbecco's modified Eagle's medium (DMEM) from Merck KGaA (Darmstadt, Germany) containing 10% FBS (Merck KGaA, Darmstadt, Germany) and 1% penicillin/streptomycin (Carl Roth GmbH + Co. KG, Karlsruhe, Germany) and incubated at 37 °C/5% CO_2. After approximately 72 h, cells were seeded on glass coverslips for force spectroscopy. For fluorescence imaging, cells were fixed with 4% paraformaldehyde for 15 min, permeabilized for 10 minutes with 0.2% Triton in PBS, and stained with TRITC-conjugated phalloidin to detect F-actin (Merck KGaA, Darmstadt, Germany) and an AF-488-conjugated monoclonal antibody against β-tubulin (Thermo Fisher Scientific, Waltham, MA) and counterstained with DAPI (ThermoFisher Scientific, Waltham, MA). We have blocked non-specific binding by means of 3% bovine serum albumin (BSA) in PBS, followed by one hour of dye-loading with a ratio of 1:1000 labels diluted in 3% blocking solution.

Imaging and spectroscopy were performed with a Bruker Icon atomic force microscope (Bruker AXS, Santa Barbara, CA) in the PeakForce tapping mode, in which the feedback loop controls the z-height of piezo to keep the maximum cantilever deflection (force) constant during each oscillation cycle. Soft sharp tip probes (pyramidal shapes with a tip radius $R = 20$ nm and a half-opening cone angle of $\alpha = 40°$) with a nominal force constant of 0.02 N/m (non-conductive silicon nitride rectangular shaped microlevers MLCT-BIO-DC-B from Bruker) and colloidal silicon oxide probes (sphere with a radius $R = 1\,\mu$m) with a nominal force constant of 1.7 N/m (CSC12 from MikroMasch, Sofia, Bulgaria) were used for determining the mechanical properties of the cells. The exact force constant was obtained by the thermal noise method.[19] Data processing and fitting of the elastic moduli and Gaussian distribution were performed using Igor pro 6.37

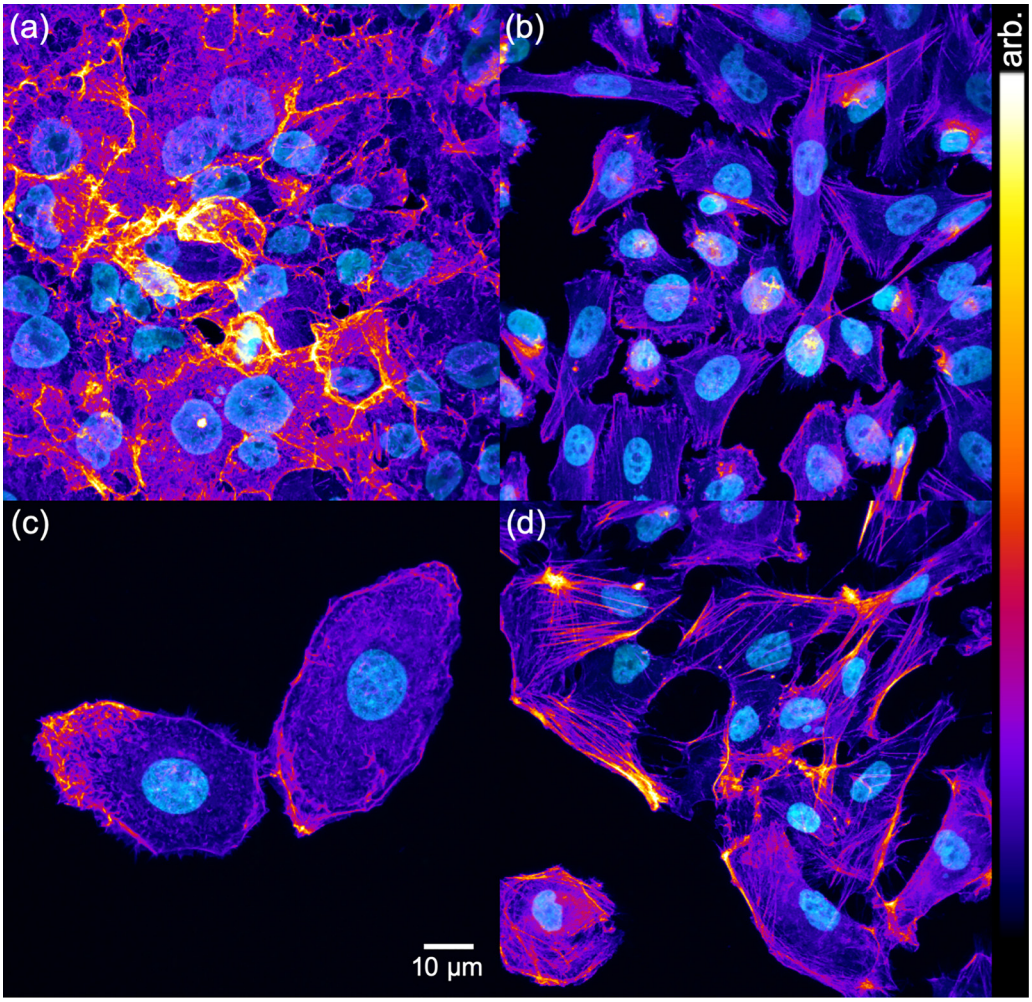

FIG. 1. Representative confocal fluorescence microscopy maximum Z-projections of (a) the PLC/PRF/5 liver cancer cell line, (b) the HS695T skin cancer cell line, (c) the BT20 breast cancer cell line, and (d) the Calu_1 lung cancer cell line, which were stained with TRITC-conjugated phalloidin to visualize (F)-actin and an AF-488-conjugated monoclonal antibody against β-tubulin (*cf.* Fig. S1) and counterstained with DAPI. For clarity and to highlight the structural malformation of the cytoskeleton, the color scale refers to the intensity of actin labels superimposed by the blueish coloration representative for the nuclei.

(WaveMatrics, Inc, Portland, OR), and image processing and analysis were done with Nanoscope Analysis 1.8 (Bruker AXS, Santa Barbara, CA).

Fluorescence imaging was accomplished using a Leica TCS SPE confocal point scanner mounted on a Leica DMi8 stand and equipped with a 63×/1.30 ACS APO Oil CS 0.17/E,0.16 objective, a solid-state ruby laser module with 405 nm, 488 nm, and 561 nm excitation lasers, and a Leica SP detector. Images were analyzed with Fiji (https://imagej.net/Fiji).

To understand the malformation of cytoskeleton components in cancerous epithelial cells under investigation, we acquired confocal fluorescence microscopy images of PLC/PRF/5 cells [henceforth designated as liver cancer cells, Fig. 1(a)], HS695T cells [skin cancer cells, Fig. 1(b)], BT20 cells [from ductal carcinoma, henceforth designated as breast cancer cells, Fig. 1(c)], and Calu_1 cells [lung cancer cells, Fig. 1(d)], which were stained with TRITC-conjugated phalloidin to visualize (F)-actin and an AF-488-conjugated monoclonal antibody against β-tubulin and counterstained with DAPI. Note that Fig. 1 shows the TRITC-conjugated phalloidin density distribution representative for the actin density (dark = low density and bright = high density) and the locations of the nuclei in light blue.

The liver cancer [Fig. 1(a)] and breast cancer cells [Fig. 1(c)] were characterized by a fair bit loss of dynamic filaments as concluded from the distribution of labeled actin, in particular their scarce appearance in the cell core region and its close vicinity and the unshaped dispersion. Contrary, skin cancer cells [Fig. 1(b)] depicted a near-normal formation of cytoskeleton components and lung cancer cells with a relatively low amount of well aligned dynamic filaments. Furthermore, the liver cancer cells attract attention because of their large dominant nuclei with respect to the overall cell sizes, leading to a relatively large nuclei portion in relation to cytoplasm volume when compared with other cancer cell lines. The actin and tubulin distributions within the cells is closely related as can be deduced from the fluorescence images presented in Fig. S1 (supplementary material).

To establish a relationship between the cytoskeleton characteristics and the overall mechanical properties of the cell lines, we further imaged the four carcinoma cell lines via the sharp tip (shown in Fig. 2) by PFT-AFM with a setpoint force of 1 nN that was the optimum force showing appropriate force-distance dependency for fitting to the Hertz contact mechanics model, the amplitude of 300 nm, and the driving frequency of 250 Hz. The analysis of the distribution of the elastic moduli in concert with the height profile on the three cell lines of skin, breast, and lung cancer, which have an acceptable portion of the nucleus to cytoplasm ratio, vividly shows the brunt of the stiff substrate in the locations of the decreased cell height with the values of about 250 kPa, >100 kPa, and 50 kPa, respectively [shown in Figs. 2(f), 2(i), and 2(l)], which are considerably larger than those of the nuclei regions and reasonably too large for soft cell tissue. The integrity of the elasticity values revealed by PFT-AFM was confirmed based on single force-distance curve fitting (see Fig. S2 in the supplementary material). On the other hand, the majority of the liver cancer cell population shows protuberant enlarged nuclei with a lack of cytoskeleton to support the cell structure [shown in Figs. 2(a) and 2(b) in concert with fluorescence images in Fig. 1(a)]. We obtained a value for the elastic modulus of approximately 10 kPa at the rim of the nucleus and approximately 50 kPa in the center of the nucleus [shown in Fig. 2(c)].

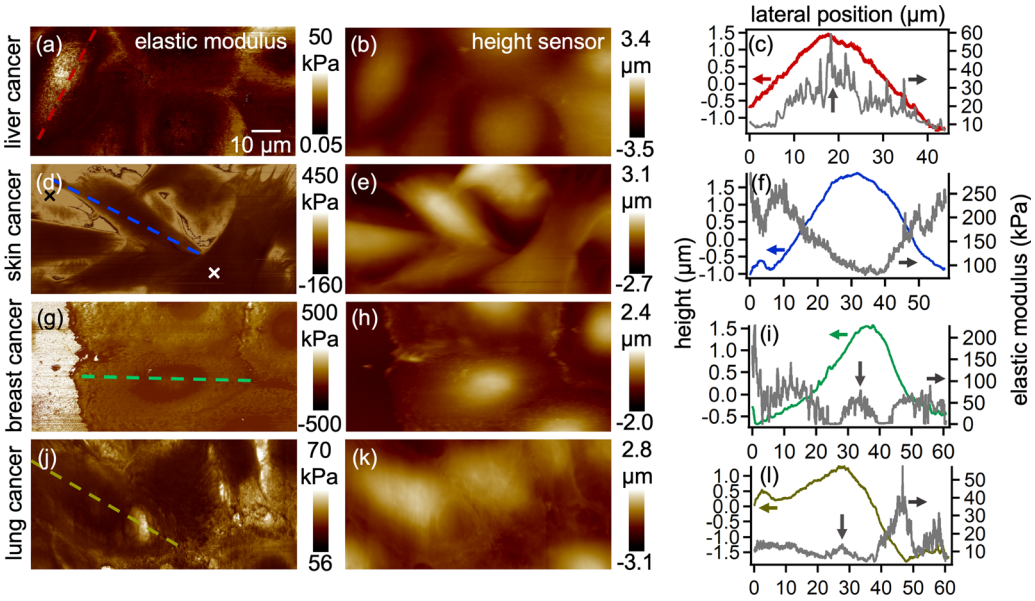

FIG. 2. AFM measurement via sharp-tip cantilevers. (a) Elastic modulus, (b) height sensor maps, and (c) height profile and elastic modulus distribution obtained from a line marked on image (a), on PLC/PRF/5. (d) Elastic modulus, (e) height sensor maps, and (f) height profile and elastic modulus distribution obtained from a line marked on image (d), on HS695T. (g) Elastic modulus, (h) height sensor maps, and (i) height profile and elastic modulus distribution obtained from a line marked on image (g), on BT20. (j) Elastic modulus, (k) height sensor maps, and (l) height profile and elastic modulus distribution obtained from a line marked on image (j) on Calu_1. The arrows on images (c), (i), and (l) show the higher elastic modulus sensed by the tip in the center of the nucleus. Note that the colored lines refer to the height values (left axis) and the gray lines to the elastic modulus values (right axis). The integrity of the elasticity values revealed by the PeakForce tapping was confirmed based on the single force-distance curve fitting, which were taken at the location marked with crosses in (d) (see Fig. S2 in the supplementary material).

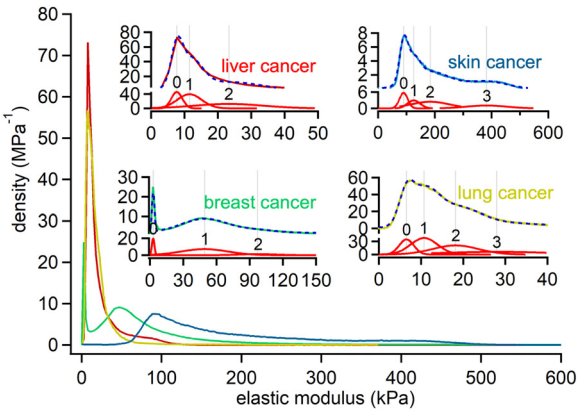

FIG. 3. Elastic modulus histograms measured via sharp-tip cantilevers on HS695T (skin cancer, blue line), BT20 (breast cancer, green line), PLC/PRF/5 (liver cancer, red line), and Calu_1 (lung cancer, yellow line) cell lines. The curves were analyzed by multiple peaks fitting via the software Igor to Gaussian distribution (insets). The fitting peaks are shown in red in the insets and the resulting fitting curves as blue dashed lines, overlaid on the correlated moduli curves.

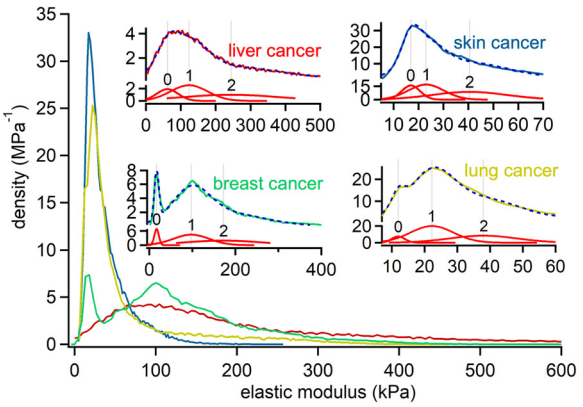

FIG. 4. Elastic modulus histograms measured via colloidal probe cantilevers on HS695T (skin cancer, blue line), BT20 (breast cancer, green line), PLC/PRF/5 (liver cancer, red line), and Calu_1 (lung cancer, yellow line) cell lines. The curves were analyzed by multiple peak fitting via the software Igor to Gaussian distribution (insets). The fitting peaks are shown in red in insets and the resulting fitting curves as the blue dashed line, overlayed on the correlated moduli curves.

Higher values in the center of the nucleus compared to the rim can also be found in the breast and lung cancer cell line elastic modulus distribution [marked by arrows in Figs. 2(c), 2(i), and 2(l)] at which cytoskeletal malformation can be observed on cells [(shown in Figs. 1(c) and 1(d)]. The histogram of distribution of elastic moduli via the sharp tip (shown in Fig. 3) has been obtained on each image of the four cell lines containing a number of cells and was analyzed by multiple peaks fitting to Gaussian distribution with the software Igor (Fig. 3 insets). It exhibits mainly two prominent peaks that are correlated with the mechanical properties of the nucleus and its periphery. The peaks that are showing the highest elastic values mainly bear the impact of stiff substrate stress reflection caused by the tip load when cross-checked with the distribution of elastic moduli on cells. These values should be interpreted with due care to not be correlated with the cell cytoskeleton, and hence, we took the mid peaks as representatives of the cytoskeleton with the elastic moduli value of about 11 kPa for liver and lung cancer cells of about 50 kPa for breast cancer cells and values between 100 and 200 kPa for the skin cancer cells. Comparing the histogram values with the distribution of elastic moduli derived from a profile drawn on the cells on all four investigated cell types shows the first peak on the histogram as a representative for a nuclei region value of approximately 100 kPa for the skin cancer cell line and <10 kPa for the three cell types of liver, breast, and lung cancer cells that show fewer formation of cytoskeleton to support the cell core and hence the nearly absolute value of the nucleus. Liver cancer cells depict the highest density value on the nuclei peak about 75 MPa^{-1}, which affirms the cell characteristics of highly enlarged prominent nuclei and scarce amount of cytoplasm compared to the other three cell lines. On the other hand, depicting the highest value of elastic moduli on skin cancer is in line with relatively normal formation of cytoskeleton compared to the others.

We imaged the four carcinoma cell lines via the colloidal probe with the set point of 10 nN that was the optimum force showing appropriate force-distance dependency for fitting to the Hertz contact mechanics model, the amplitude of 300 nm, and the driving freqeuncy of 250 Hz. For the analysis of the elastic moduli, we used histograms (shown in Fig. 4) where the curves were evaluated by multiple peaks fitting via the software Igor to Gaussian distribution (Fig. 4, insets).

The structural cell characteristics and the respective elasticity values obtained via the sharp tip and colloidal probes in the force microscopy assessment are summarized in Table I.

We assumed that the cells with fewer or in some cases lack of formation of two main cytoskeleton components such as for breast or liver cancer cells depict lower elastic modulus compared to counter cells with formation of these filaments (lung and in particular skin

TABLE I. Structural peculiarities and mechanical properties assessed by AFM using a sharp tip ($r = 20$ nm) and a colloidal probe ($r = 1$ μm).

	Cell line			
Peculiarities and mechanical properties	Breast cancer (BT20)	Liver cancer (PLC/PRF/5)	Lung cancer (Calu_1)	Skin cancer (HS695T)
Cytoskeleton characteristics	Fair bit loss	Fair bit loss	Moderate	Near-normal
Portion of the nucleus to cytoplasm	Normal ratio	Prominent large	Normal ratio	Normal ratio
$E_{\text{periphery}}$ (kPa) tip radii: **20** nm (*1* μm)	**50** (*150–250*)	**11** (*200–300*)	**11** (*30–40*)	**100–200** (*30–50*)
E_{nuclei} (kPa) tip radii: **20** nm (*1* μm)	$<$**10** (*100*)	$<$**10** (*100–200*)	$<$**10** (*20–30*)	**100** (*20–30*)

cancer cells). Using a sharp probe, this assumption is corroborated by the coarse trend of increasing elastic modulus with the increasing mechanical support of cytoskeletal cell support (see Table I, bold numbers). Using a colloidal indenter having a large tip radius of 1 μm, however, we observed that liver and breast cancer cells show a fair bit loss of dynamic filaments [see Figs. 1(a) and 1(c)], yet, on the histograms, we observed the highest value of elastic modulus of in the range of 100–300 kPa on these two cell lines. Contrary, the skin cancer cell line with near-normal formation of cytoskeleton components and the lung cancer cell line with a relatively less amount of dynamic filaments show a very low elastic modulus of about 20–50 kPa as summarized in Table I (italic numbers).

The force sensed by the tip at the cell surface and beneath is a sum of the force exerted to the cell and the force reflected at the stiff substrate caused by propagating stress. Garcia and Garcia[14] have developed a bottom effect elastic theory for various indenter geometries implementing correction terms for the cell height, which relates the force with the deformation of a cell adherent to a stiff substrate. It was demonstrated that the thinner the thickness of the cell becomes, as it is the case when the tip moves away from the nucleus toward the cell periphery, the higher the force is sensed by the tip. The effect is particularly high for spherical intenders with large tip radii. This leads to an overestimation of the elastic modulus deduced by conventional Hertz/Sneddon theory straightforwardly corrigible using additional terms up to fourth order for the force-indentation relationship.[14] Our experimental findings are in total agreement with this theory since the elasticity values measured with the colloidal probe are substantially higher than those deduced by a sharp tip for breast, lung, and liver cancer cells. The drastic overestimation of the elastic modulus using colloidal probes in comparison with sharp tips can be directly deduced from a representative comparison of force vs indentation curves (see Fig. S3 in the supplementary material), which also qualitatively demonstrates the stronger influence of large spherical tips by viscoelastic forces (compare enclosed areas by trace and retrace portions) with respect to the sharp counterparts. Moreover, we could experimentally demonstrate that for a comparison of the rigidity of cancerous cells, differences in the distribution and peculiarities of the filamentous structure have an additional non-negligible effect on the determination of elasticity values by AFM (*cf.* Table I, overestimation of elastic modulus for cells with a fair bit loss of filamentous structures). We postulate that the abundance of cytoskeleton components causes damping of the propagating stress within the cell interior and thus reduces the effect of overestimation of elasticity as it is the case for skin cancer cells with a near-normal formation of filamentous structures.

In conclusion, considering the above-mentioned arguments, although measurements via the sharp tip are still having the impact of substrate stress reflection caused by the tip load, compared to the values achieved by the colloidal tip, sharp tip cantilevers are the better choice for obtaining trustworthy values on cell monolayers attached to a stiff substrate, specifically in cancer AFM based studies in which cells show cytoskeleton abnormalities. Furthermore, for biological applications, we appeal to the manufacturers of force microscopes to implement contact mechanics models that take into account the effects of stiff substrates on soft samples that can be considered as incompressible such as cells.

See the supplementary material for the additional confocal fluorescence microscopy images of metastatic cancer cell lines and representative force vs indentation curves.

The authors thank the Deutsche Forschungsgemeinschaft (Sachbeihilfe No. DI 2176/2-1) for their financial support.

REFERENCES

[1]L. M. Rebelo, J. S. de Sousa, J. Mendes Filho, and M. Radmacher, Nanotechnology **24**, 055102 (2013).
[2]M. Plodinec, M. Loparic, C. A. Monnier, E. C. Obermann, R. Zanetti-Dallenbach, P. Oertle, J. T. Hyotyla, U. Aebi, M. Bentires-Alj, R. Y. H. Lim, and C. A. Schoenenberger, Nat. Nanotechnol. **7**, 757 (2012).
[3]P. Eaton, V. Zuzarte-Luis, M. M. Mota, N. C. Santos, and M. Prudencio, Nanomedicine **8**, 17 (2012).
[4]N. V. Bukoreshtliev, K. Haase, and A. E. Pelling, Cell Tissue Res. **352**, 77 (2013).
[5]S. Janel, M. Popoff, N. Barois, E. Werkmeister, S. Divoux, F. Perez, and F. Lafont, Nanoscale **11**, 10320 (2019).
[6]A. Amiri, F. Hastert, L. Stühn, and C. Dietz, Nanoscale Adv. **1**, 4853 (2019).
[7]L. Stuhn, A. Fritschen, J. Choy, M. Dehnert, and C. Dietz, Nanoscale **11**, 13089 (2019).
[8]M. Gupta, B. R. Sarangi, J. Deschamps, Y. Nematbakhsh, A. Callan-Jones, F. Margadant, R. M. Mége, C. T. Lim, R. Voituriez, and B. Ladoux, Nat. Commun. **6**, 7525 (2015).
[9]E. C. Faria, N. Ma, E. Gazi, P. Gardner, M. Brown, N. W. Clarke, and R. D. Snooka, Analyst **133**, 1498 (2008).
[10]G. Zhang, M. Long, Z. Z. Wu, and W. Q. Yu, World J. Gastroenterol. **8**, 243 (2002).
[11]J. R. Ramos, J. Pabijan, R. Garcia, and M. Lekka, Beilstein J. Nanotechnol. **5**, 447 (2014).
[12]A. J. Rice, E. Cortes, D. Lachowski, B. C. H. Cheung, S. A. Karim, J. P. Morton, and A. Del Rio Hernandez, Oncogenesis **6**, e352 (2017).
[13]P. K. Viji Babu, C. Rianna, U. Mirastschijski, and M. Radmacher, Sci. Rep. **9**, 12317 (2019).
[14]P. D. Garcia and R. Garcia, Biophys. J. **114**, 2923 (2018).
[15]C. Valero, S. Navarro, D. Navajas, and J. M. Garcia-Aznar, J. Mech. Behav. Biomed. Mater. **62**, 222 (2016).
[16]Y. Ding, G. K. Xu, and G. F. Wang, Sci. Rep. **7**, 45575 (2017).
[17]A. Raman, S. Trigueros, A. Cartagena, A. P. Z. Stevenson, M. Susilo, E. Nauman, and S. A. Contera, Nat. Nanotechnol. **6**, 809 (2011).
[18]M. O. Krisenko, A. Cartagena, A. Raman, and R. L. Geahlen, Biochemistry **54**, 60 (2015).
[19]H. J. Butt and M. Jaschke, Nanotechnology **6**(1), 1 (1995).